This is a peer-reviewed, author's accepted manuscript of the following research article:
Chen, J., Fyffe, B., Han, D., & Yang, S. (2022).
Predicting mixed mode damage propagation in snowpack using the extended cohesive damage element method.
Theoretical and Applied Fracture Mechanics, 122, [103567]. https://doi.org/10.1016/j.tafmec.2022.103567

Predicting Mixed Mode Damage Propagation in Snowpack Using the Extended Cohesive Damage Element Method

Jiye Chen[1*], Blair Fyffe[2], Dawei Han[3] and Shangtong Yang[4]
[1]School of Civil Engineering Science and Surveying, University of Portsmouth, UK.
[2]Scottish Avalanche Information Service, UK
[3]Department of Civil Engineering, University of Bristol, UK
[4]Department of Civil and Environmental Engineering, University of Strathclyde, UK

Key words: Extended Cohesive Damage Element, Mixed Mode Damage Propagation, Propagation Saw Test, Snowpack Failure Mechanism.

Abstract

A novel extended cohesive damage element method is used to develop a numerical snowpack model to study the fundamental damage mechanisms of snowpack under external drivers and to investigate multiple mixed mode damage propagation within the snowpack. A new mixed mode damage criterion is introduced to account for tensile and shear fractures as well as compressive crushing together with shear crack for approximating the mixed mode damage initiation and propagation in the weak layer in snowpack. A propagation saw test (PST) is considered to understand basic damage involution in snowpack under self-weight related bending. The nonlinear fracture modelling prediction agrees with the PST sample well. This paper provides a potential approach as a predictive method using the extended cohesive damage element for forecasting slab avalanches in snow terrain according to weather forecast and planned human activities in the future.

1. Introduction

Snow avalanches are among the most destructive natural disasters and result in the loss of life and economic damage in mountainous regions worldwide. Snow slab avalanches account for the overwhelming majority (around 90%) of avalanche-related fatalities in backcountry users. Slabs can vary in thickness from a few centimetres to three metres, usually less than 1 m. The observed ratio between width and thickness of the slab varies between 10 and 10^3. One of the main goals of snow avalanche research is to forecast the natural or induced mechanical failure of a sloping layered snowpack in order to estimate the potential damage and thus to be able to conduct risk-oriented planning. Forecasting snow slab avalanches is a fundament to be able to mitigate the risk from this natural hazard. At present, a single avalanche event cannot be predicted in time and space [1]. Much about the release process remains unknown, mainly because of the highly variable, layered character of the snowpack, a highly porous material that exists close to its melting point. The complex interaction between terrain, snowpack, and meteorological conditions leading to avalanche release is commonly described as avalanche formation. The release process can be studied and modelled. The modelling approach relies heavily on snow mechanics and snow properties, including misconstruction. While the effect of meteorological conditions or changes on the deformational

behaviour of snow is known in qualitative or semiquantitative manner, the knowledge of the quantitative relation between snow misconstruction and mechanical properties is limited.

There have many investigations into avalanches during the past two decades. mGEODAR [2] is radar imaging technology for detection of avalanches and the characterization of avalanche flow. Distributed acoustic sensing has been used for avalanche monitoring and understanding the release mechanisms and propagation dynamics. These sensor-based technologies would not be appropriate for forecasting avalanches because they tend to have insufficient lead times and insufficient spatial distributions. A statistical approach such as MEWS [3] uses telemetry multi-sensor device such as radar to collect data in hazard zone and then uses AI technology to predict trigging condition of avalanches. Its accuracy almost depends on senor resolution. Snow is a brittle material and in the majority of cases release progresses rapidly once failure is initiated. It would be challenging for a multi-sensor device to detect enough data to predict the moment of release, and even if it were able to it may be too late for forecasting and planning mitigation. Based on the MEWS technology, some physic detecting stations with installed telemetry multi-sensor devices are established. However, it would not be easy to establish global physic sensor network for detecting avalanches.

The material point method (MPM) [4] uses an elastoplasticity model to simulate an existing avalanche with given information for location of slab avalanche and weak layer, and to simulate the dynamic release processes of a slab avalanche and the motion of avalanches from release to deposition. Unlike simulating the physical snow fracture propagation in snow stratigraphy, MPM would not be a predictive tool to forecast the initiation and location of avalanches in time and space. Classical fracture mechanical models have been applied to explain the fracture mechanism. Micromechanical models including two competing processes (damage and sintering) have also been applied to avalanche release. However, there are knowledge gaps between the various processes which lead to the release of the snow slab: snow deformation and failure, damage accumulation, fracture initiation, and fracture propagation. Simultaneously, classical fracture mechanical model difficultly considers the spatial variability that affects damage, fracture initiation and location, and fracture propagation as avalanche process [1]. The French model Crocus is part of the operational forecasting model chain SAFRAN-Crocus-ME´PRA, which includes stability evaluation and simplistically takes into account terrain (aspect and elevation) [5]. The Swiss model SNOWPACK is primarily microstructure-based and simulates the snow cover evolution in level study plots [6]. It runs operationally to calculate parameters such as the new snow depth and drift index for the Swiss avalanche warning service. However, these two models would not be spatial and temporal calculation for fracture initiation and fracture propagation in a snow terrain model. Most numerical modelling has used classical finite element models to calculate stress, strain, and strain rates for complex geometry, including layering and irregularities in the snowpack [7 – 10]. Other numerical models have used the finite difference method to solve the stress-strain relations for snow stability conditions using a simple stress failure criterion and a simplified concave slope [11]. DEM (Discrete

Element Method) [12], FVM (Finite Volumes Method) [13] fail to model the entire avalanche process, from quasi-static failure initiation to dynamic crack propagation and flow at the slope scale. These approaches would not be suitable to explain the complicated fracture mechanisms of the snowpack and unable to predict the crack initiation or fracture propagation. Computational fluid mechanics approach and hydrodynamics approach, e.g., D2FRAM (Dynamical Two-Flow-Regime Avalanche Model) can only model avalanche process as a fluid flow or snow powder flow process after snowpack separated by fractures as a post fracture process. Recently, Machine learning methods (MLM) including support vector machine (SVM) and multivariate discriminant analysis (MDA) [14] were used to map the hazard zones in an avalanche zone in terms of three main historic categories of data; avalanche occurrence locations, meteorological factors, and terrain characteristics. A total 14 parameters are involved. Obviously, MLM is used as a statistical approach to provide hazard zone mapping and would not predict the initiation and propagation of snow avalanches.

Slab avalanche release is a complex physical fracture process which involves tensile and shear crack initiation and propagation, and mixed mode damage propagation with compressive crushing and shear crack in the weak layer. Aforementioned numerical modelling approaches used in the study of snow fracture mechanisms are not fully capable to predict snowpack fracture propagation, especially the mixed mode damage propagation in the weak layer, and to precisely predict detailed mixed mode damage propagation and corresponding failure response. A highly efficient numerical predictive tool is needed to cope with this problem. In computational damage mechanics, highly efficient simulation of multicrack propagation in nonlinear materials has attracted a lot of attention in academia in the last decade. There have been many approaches based on the Partition of Unity Method (PUM) [15] to conduct the arbitrary discontinuity problems in engineering or geotechnical materials and structures. Among PUM based approaches, the eXtended Finite Element Method (XFEM), as a combination of the classical FEM and PUM, was originally introduced by Belytschko et al. [16] and subsequently enhanced by Moës et al. [17]. By enriching the classical piecewise polynomial approximation basis within FEM framework, XFEM is capable of conducting thorough computational characterization for non-smooth features within a discontinuous medium. The existence of a discontinuity can be introduced, irrespective of its size and specific orientation. Thus, no mesh regeneration is needed during discontinuity evolution, and element boundary would no longer need to be the discontinuity surface, which is a significant benefit to the work of modelling multicrack propagation. The major drawback of the above mentioned PUM related methods are the enriched terms as additional degree of freedoms (DoFs) or nodes bring expensive computational cost. Sometimes, it can be impossible to achieve convergent solutions when encountering high nonlinearity [18]. In consideration of this drawback, a novel Extended Cohesive Damage Model (ECDM) was developed by the lead author of this study in 2017 to describe the multicrack propagation in engineering materials [19]. The ECDM is proved to be a highly efficient approach in computational nonlinear damage mechanics for simulating multicrack propagation [20-24]. The developed ECDM has the following specific features: (a) enriched DoFs are eliminated from the fully

condensed equilibrium equations; (b) the cohesive damage law is embedded into the condensed equilibrium equation at the element level for characterising micro damage; (c) the effects from the enriched DoFs and the cohesive characteristic are accounted into the final condensed formulation; (d) the derived formulations are presented with the standard FEM displacements only; (e) a novel equivalent damage scalar as a function of strain field is employed based on the thermal dissipation, which enables the model conforms with thermodynamic consistency. The ECDM is a computationally efficient approach since only standard DoFs are needed.

The extended cohesive damage element (ECDE) introduced in this paper is a continuation of the ECDM concept, but incorporates a new mixed mode damage criterion to precisely simulate tensile and shear fracture as well as mixed mode damage process with compressive crushing and shear crack propagation in the weak layer in snowpack. The proposed ECDE aims to fundamentally study dry snow slab avalanche mechanisms, and to show that dealing with a highly porous media and processes covering several orders of scale, from the size of a bond between snow grains to the size of a mountain slope. The ECDE aims to predict the initiation, location and propagation of slab avalanches. The new mixed mode damage criteria will be embedded into the ECDE to approximate detailed mixed mode damage involution mechanisms in snowpack under external loading conditions. The ECDE is a PUM based and a condensed discrete formulation through eliminating the enriched degree of freedoms (DoFs). This paper will introduce the theory and equations of the ECDE, followed by an application of the ECDE in the prediction of multiple mixed mode damage propagation during a propagation saw test (PST) [4, 31]. Finally, this paper will give conclusions and discuss its potential application in establishing an early warning system of slab avalanches under weather forecast and human activities in the future.

2. Basic formulations of the ECDE

2.1 Kinematics of cohesive crack problem

In a 2D continuum $\Re^2$, consider a discontinuous physical domain $\Omega \in \Re^2$, whose outward normal vector **n,** intersected by a cohesive crack Γ_d with normal vector **m**, as shown in Fig. 1(a). Such that the domain is divided into two subdomains represented as Ω^+ and Ω^-, respectively, as shown in Fig. 1(b). The crack results in the presence of two new consistent internal boundaries Γ_d^+ and Γ_d^-. The prescribed external load $\bar{\mathbf{t}}$ is imposed on boundary Γ_t and the displacement $\bar{\mathbf{u}}$ is assumed on boundary Γ_u. Omitting the body forces, the strong form of the equilibrium equation can be written as:

$$\mathrm{Div}\,\boldsymbol{\sigma} = 0 \qquad (1)$$

where the second-order tensor $\boldsymbol{\sigma}$ denotes the stress field in the bulk domain $\Omega = \Omega^+ \bigcup \Omega^-$. The boundary conditions for the domain Ω are:

$$\boldsymbol{\sigma} \cdot \mathbf{n} = \bar{\mathbf{t}} \ (\text{on } \Gamma_t) \qquad (2)$$

$$\mathbf{u} = \bar{\mathbf{u}} \quad (\text{on } \Gamma_u) \qquad (3)$$

Due to the presence of cohesive segment, boundary conditions imposed on the discontinuous boundaries Γ_d^+ and Γ_d^- are given below.

$$\mathbf{t}^+ = \boldsymbol{\sigma}^+ \cdot \mathbf{m}^+ = -\mathbf{t} \ (\text{on } \Gamma_d^+) \qquad (4)$$

$$\mathbf{t}^- = \boldsymbol{\sigma}^- \cdot \mathbf{m}^- = \mathbf{t} \ (\text{on } \Gamma_d^-) \qquad (5)$$

According to the traction-separation law [25], the traction attributing to the cohesive segment between crack surfaces can be obtained from the relative displacement:

$$\mathbf{t} = \mathbf{t}(\delta) \qquad (6)$$

in which δ is the relative displacement between two boundaries of discontinuity. The above equation serves as a nonlinear material model when discontinuity onsets.

While the cohesive tractions are present within the specified segment of crack, the total potential of the body should take account for the contribution from cohesive tractions transferred through the crack surface. According to the principle of virtual work, the weak form of equilibrium equation based on the strong form of the equilibrium equation given in Equ. (1) can be written as:

$$\int_\Omega \left[\nabla \boldsymbol{\omega}(\mathbf{x}) : \sigma(\mathbf{u}(\mathbf{x}))\right] d\Omega - \int_{\Gamma_t} \boldsymbol{\omega}(\mathbf{x}) \cdot \bar{\mathbf{t}} \, d\Gamma - \int_{\Gamma_d^+} \boldsymbol{\omega}(\mathbf{x}) \cdot \mathbf{t}^+ \, d\Gamma - \int_{\Gamma_c^-} \boldsymbol{\omega}(\mathbf{x}) \cdot \mathbf{t}^- \, d\Gamma = 0 \qquad (7)$$

In the weak form, **ω(x)** and **u(x)** are test and solution functions, respectively.

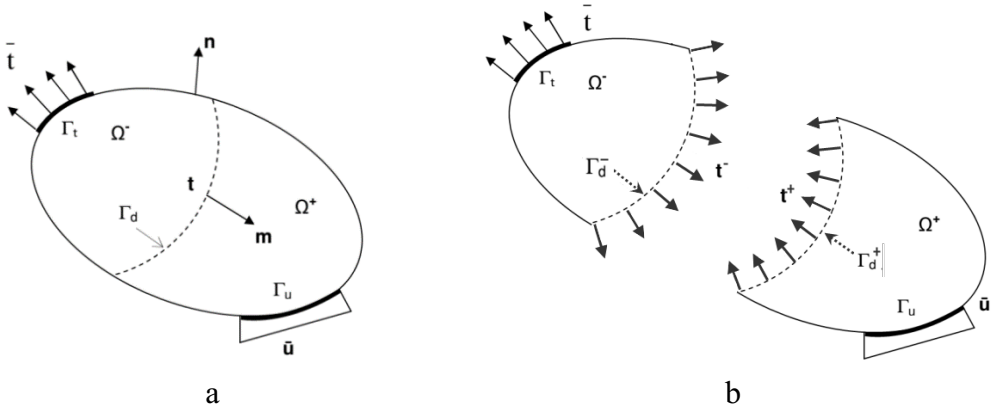

Fig 1. Notation for a 2D domain with an arbitrary discontinuity Γ_d.

2.2 Displacement filed and shifted Heaviside function

The test and trial function of the discontinuous displacement field can be given as [19]:

$$\mathbf{u}(\mathbf{x}) = \mathbf{u}^s(\mathbf{x}) + Step_{\Gamma_d}(\mathbf{x})\mathbf{a}(\mathbf{x}) \qquad (8)$$

where $\mathbf{u}^s(\mathbf{x})$ and $\mathbf{a}(\mathbf{x})$ stand for the regular displacement field and the displacement jump, respectively. $Step_{\Gamma_d}(\mathbf{x})$ is a step function characterizing the physical jump when the element is completely separated (strong discontinuities). In FEM discrete form, the approximation of displacement field can be represented as:

$$\mathbf{u}^h(\mathbf{x}) = \sum_{i\in I} N_i(\mathbf{x})\mathbf{u}_i + \sum_{i\in J} N_j(\mathbf{x})\left(\mathscr{H}_{\Gamma_d}(\mathbf{x}) - \mathscr{H}_{\Gamma_d}(\mathbf{x}_i)\right)\mathbf{a}_i \qquad (9)$$

in which $\mathscr{H}_{\Gamma_d}(\mathbf{x}) = \begin{cases} 1, & \forall \mathbf{x} \in \Omega^+ \\ 0, & \forall \mathbf{x} \in \Omega^- \end{cases}$ is a Heaviside step function. It should be noted that, in the above discretization of displacement, the shifted function $\mathscr{H}_{\Gamma_d}(\mathbf{x}) - \mathscr{H}_{\Gamma_d}(\mathbf{x}_i)$ is introduced for satisfying the *Kronecker-δ* property (i.e., $N_i(x_j) = \delta_{ij}$). The introduction of shifted Heaviside function does not alter the approximating basis while simplifies the implementation attributing to that resulting enrichment vanished in elements which are not cut by the discontinuity [19].

2.3 Discrete and condensed equilibrium equations

Using the weak form of equilibrium equation from Bubnov-Galerkin method, the discrete form of equilibrium equation for static analysis can be written as shown in Equ. (10).

$$\begin{bmatrix} \mathbf{K}^{uu} & \mathbf{K}^{ua} \\ \mathbf{K}^{au} & \mathbf{K}^{aa} \end{bmatrix} \begin{bmatrix} \mathbf{u} \\ \mathbf{a} \end{bmatrix} = \begin{bmatrix} \mathbf{f}_{ext}^{u} \\ \mathbf{f}_{ext}^{a} \end{bmatrix} \qquad (10)$$

where $\mathbf{K}^{uu}$ and $\mathbf{K}^{aa}$ are the stiffness matrices associated with the standard FE approximation and the enriched approximation, respectively; $\mathbf{K}^{ua}$ or $\mathbf{K}^{au}$ account for the coupling between the standard FE approximation and the enriched approximation; $\mathbf{f}_{ext}^{\mathbf{u}}$ and $\mathbf{f}_{ext}^{a}$ are the equivalent nodal force vectors for standard FEM DoFs and enriched DoFs, respectively; **u** denotes the standard DoFs while **a** denotes the enriched DoFs.

As aforementioned, the crack shown in Fig. 1 is a cohesive crack, and the discontinuous boundary is a cohesive crack boundary. Thus, in Equ. (10), the equivalent nodal force vectors can be expressed as:

$$\begin{aligned} \mathbf{f}_{ext}^{u} &= \int_{\Gamma^h} \mathbf{N}^T \bar{\mathbf{t}} d\Gamma \\ \mathbf{f}_{ext}^{a} &= \int_{\Gamma^h} \mathbf{N}^T (\mathrm{H}_{\Gamma_d}(x,y) - \mathrm{H}_{\Gamma_d}(x_i,y_i)) \bar{\mathbf{t}} d\Gamma + \mathbf{f}_{coh} \end{aligned} \qquad (11)$$

Because of the existence of cohesive segment, the internal nodal force vector due to cohesive traction **t** on the crack surface Γ_d can be expressed as:

$$\begin{aligned}\mathbf{f}_{coh} &= \int_{\Gamma_{d^+}} \left(\mathscr{H}_{\Gamma_d}(x,y) - \mathscr{H}_{\Gamma_d}(x_i,y_i) \right) \mathbf{N}^T \mathbf{t} d\Gamma + \int_{\Gamma_{d^-}} \left(\mathscr{H}_{\Gamma_d}(x,y) - \mathscr{H}_{\Gamma_d}(x_i,y_i) \right) \mathbf{N}^T (-\mathbf{t}) d\Gamma \\ &= \int_{\Gamma_d} \mathbf{N}^T \mathbf{t} d\Gamma \end{aligned} \tag{12}$$

The integration of the internal nodal force vector due to cohesive traction **t** shown in Equ. (12) can be obtained by numerical integration regarding to the cohesive stress on the crack surface Γ_d.

In this work, the standard Gaussian integration scheme are used, that is,

$$\mathbf{f}_{coh} = \int_{\Gamma_d} \mathbf{N}^T \mathbf{t} d\Gamma = \sum_{i=1}^{n} \mathbf{N}^T(\xi_i) \mathbf{t}(\xi_i) \mathrm{w}(\xi_i) \tag{13}$$

where ξ_i is the coordinate of Gauss integration point *i* ($1 \le i \le n$); $\mathrm{w}(\xi_i)$ is a weight function. Substituting the expression of equivalent nodal force vector in Equ. (11) into Equ. (10) results Equ. (14):

$$\begin{bmatrix} \mathbf{K}^{uu} & \mathbf{K}^{ua} \\ \mathbf{K}^{au} & \mathbf{K}^{aa} \end{bmatrix} \begin{bmatrix} \mathbf{u} \\ \mathbf{a} \end{bmatrix} = \begin{bmatrix} \mathbf{f}_u^{ext} \\ \int_{\Gamma_d} \mathbf{N}^T (H_{\Gamma_d}(x,y) - H_{\Gamma_d}(x_i,y_i)) \bar{\mathbf{t}} d\Gamma \end{bmatrix} + \begin{bmatrix} 0 \\ \mathbf{f}_{coh} \end{bmatrix} \tag{14}$$

To be able to reach a fully condensed equilibrium system, the additional enrichment term **a** is eliminated, thus the equilibrium equation with the standard FEM unknown quantities can be consequently obtained as shown in Equ. (15):

$$\left(\mathbf{K}^{uu} - \mathbf{K}^{ua} \left(\mathbf{K}^{aa} \right)^{-1} \mathbf{K}^{au} \right) \mathbf{u} = \mathbf{f}_{ext}^{u} - \mathbf{K}^{uu} \left(\mathbf{K}^{aa} \right)^{-1} \mathbf{M} \mathbf{f}_{ext}^{u} - \mathbf{K}^{ua} \left(\mathbf{K}^{aa} \right)^{-1} \mathbf{f}_{coh} \tag{15}$$

where, **M** is a transformation matrix to link the $\mathbf{f}_{ext}^{a}$ and $\mathbf{f}_{ext}^{\mathbf{u}}$ as below.

$$\mathbf{f}_{ext}^{a} = \mathbf{M} \mathbf{f}_{ext}^{u} \tag{16}$$

The exact expression of **M** can be found in author's previous work [19]. It should be noted that in the most case **M** is zero because there is no external load applied on the cohesive crack. Thus Equ. (15) can be rewritten as:

$$\left(\mathbf{K}^{uu} - \mathbf{K}^{ua} \left(\mathbf{K}^{aa} \right)^{-1} \mathbf{K}^{au} \right) \mathbf{u} = \mathbf{f}_{ext}^{u} - \mathbf{K}^{ua} \left(\mathbf{K}^{aa} \right)^{-1} \mathbf{f}_{coh} \tag{17}$$

This ECDE formulation is a lower order equilibrium system comparing to the XFEM in ABAQUS, which permits nodal displacement calculation of the cracked element using standard FEM DoFs only. This proposed rigorous mathematical procedure can fully cover the damage evolution from a weak discontinuity to a strong discontinuity.

2.4 Cohesive damage model for the discontinuity

The cohesive damage law is employed here to characterize the nonlinear cohesive segment evolution transferred across the discontinuity. The cohesive traction $\mathbf{t}_{coh} = \left[t_n, t_s\right]^T$ contains two components, which are normal traction and shearing traction, respectively. As a function of the damage scalar *d* in both normal and tangential directions at crack surface, $\mathbf{t}_{coh}$ decreases monotonically to zero, which is mathematically expressed by Equ. (18) [25, 26].

$$\mathbf{t}_{coh} = (1-d)\mathbf{t}_0 \tag{18}$$

where $\mathbf{t}_0$ is the traction when crack initiates. The cohesive tractions in Equ. (18) are calculated at crack surface in the direction *n* and *s*, respectively. In the implementation, the transformation of coordinates from local coordinate *n* and *s* to global coordinate *x* and *y* is necessarily required and expressed by Equ. (19).

$$\mathbf{t}_{coh}^{global} = \left[\mathbf{R}\right]\mathbf{t}_{coh}^{local} \tag{19}$$

where the transformation matrix **R** is given by Equ. (20).

$$\left[\mathbf{R}\right] = \begin{bmatrix} -\sin\theta & \cos\theta \\ \cos\theta & \sin\theta \end{bmatrix} \tag{20}$$

where θ is the angle between the coordinate *n*-*s* and the coordinate *x*-*y*. There is not a physical relative displacement $\Delta\delta$ before a crack formed within elements. Two schemes are widely used in approximating the evolution of cohesive failure, which are linear softening scheme and exponential softening scheme, respectively, as shown with the traction-relative displacement $\Delta\delta$ functions in Figs. 2(a) and 2(b). Nevertheless, as demonstrated in the ECDE equilibrium, eliminating the enriched DoFs has resulted a vanishing of relative displacement $\Delta\delta$ in the ultimate solution, which brings difficulties in recognizing the softening status of cohesion.

In this developed ECDE, a new equivalent damage scalar based on strain energy dissipation is used to avoid the appearance of the additional DoFs related displacement gap $\Delta\delta$. In the ECDE based FEM modelling, it is expected that the evolution of cohesive zone will present a micro behavior of strain softening, so that the strain energy dissipation shown in Figs. 2(c) and 2(d) due to occurrence of fracture is supposed to be equivalent to the released work done by cohesive traction or released fracture energy shown in Figs. 2(a) and 2(b). Based on this consideration, the macro performance of material with bilinear cohesive softening law and exponential cohesive softening law is supposed to follow the specified schemes with similar curve shape, as demonstrated in Figs. 2(c) and 2(d), respectively. Therefore, in the utilization of the ECDE, the damage scalar can be expressed equivalently by a released strain energy using linear softening or exponential softening law as shown in Equ. (21).

$$d = \frac{\int_\Omega \frac{1}{2}\sigma^0 \varepsilon d\Omega - \int_\Omega \frac{1}{2}\sigma\varepsilon^0 d\Omega}{G_c l_{crack}}$$

or

$$d = \frac{\int_\Omega A\left\{\exp\left[\frac{\sigma^0}{A}(\varepsilon^0 - \varepsilon)\right] - 1\right\} d\Omega + \int_\Omega \frac{1}{2}\left(\sigma^0\varepsilon^0 - \sigma\varepsilon\right) d\Omega}{G_c l_{crack}} \quad (21)$$

where, σ^0 and ε^0 are the material strength and the initial damage strain respectively when damage onsets; l_{crack} is elemental crack length from the start point to the end point of the crack in a cracked element. The damage status is considered to be coincident along the elemental crack length; G_c is fracture energy; A is a parameter expressed as $\frac{G_c l_{crack}}{S} - \frac{1}{2}\sigma^0\varepsilon^0$ in which S is the total area under the curve of softening damage law shown in Figs. 2(c) and 2(d). Herein a softening constitutive law is used for reducing the cohesive traction, i.e. $\sigma = (1-d)\sigma^0$. Bringing this calculation into Equ. (21), an explicit expression of the equivalent damage scalar can be achieved as shown below:

$$d = \frac{\int_\Omega \frac{1}{2}\sigma^0 \varepsilon d\Omega - \int_\Omega \frac{1}{2}\sigma^0\varepsilon^0 d\Omega}{G_c l_{crack} - \int_\Omega \frac{1}{2}\sigma^0\varepsilon^0 d\Omega}$$

or

$$d = \frac{\int_\Omega A\left\{\exp\left[\frac{\sigma^0}{A}(\varepsilon^0 - \varepsilon)\right] - 1\right\} d\Omega + \int_\Omega \frac{1}{2}\sigma^0\left(\varepsilon^0 - \varepsilon\right) d\Omega}{G_c l_{crack} - \int_\Omega \frac{1}{2}\sigma^0\varepsilon d\Omega} \quad (22)$$

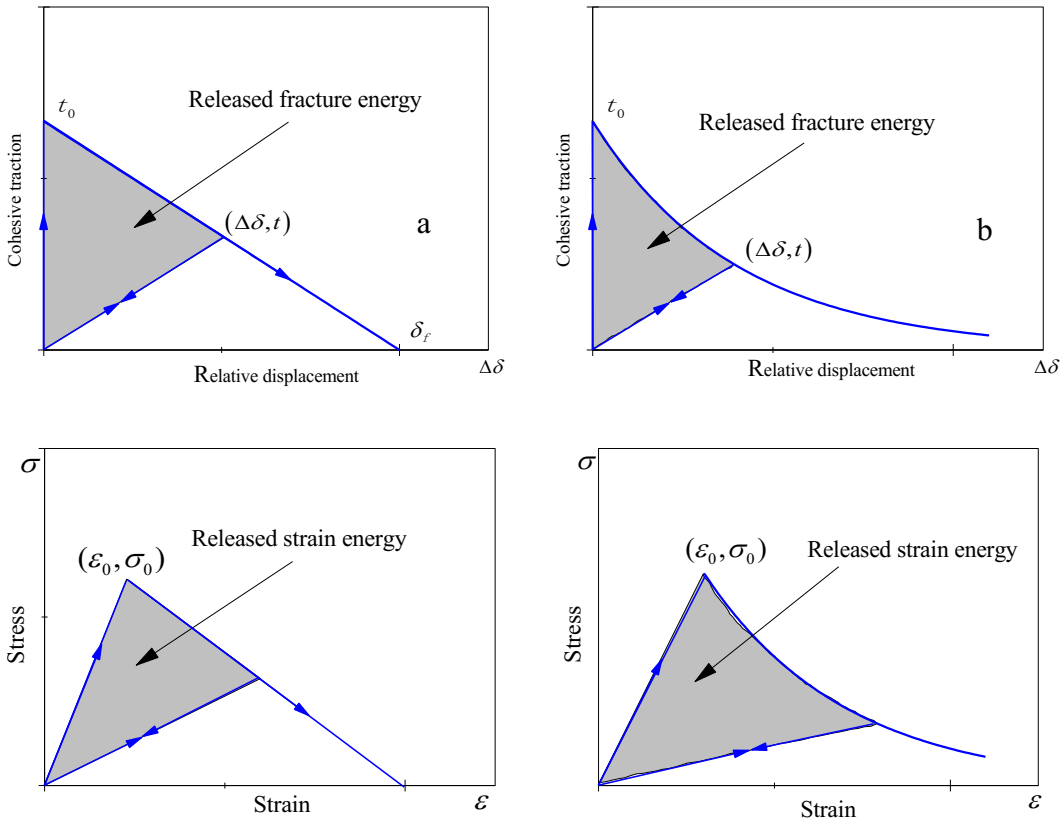

Fig. 2. (a) Linear cohesive damage law; (b) Exponential cohesive damage law;
(c) Linear material constitutive behavior; (d) Exponential material constitutive behavior.

It should be noted that the damage scalar *d* in Equ. (22) is a function of strain field obtained with conventional DoFs only, with which the requirement to calculate the enriched DoFs related displacement gap $\Delta\delta$ can be effectively avoided.

3. Numerical implementation

In most existing discrete discontinuity approaches, a vital requirement for efficient implementation is the FEM code which allows flexible variation within limited number of DoFs per node and number of integration points per element. Attributing to the elimination of enriched DoFs, the ECDE can overcome this restriction and be easily integrated into commercial FEM software. Another advantage of the ECDE is that it can relieve users from utilizing a sophisticated global tracking algorithm, such as the level-set functions in XFEM for a propagating discontinuity. Consequently, the large pre-calculations can be avoided when discontinuity is activated in a narrow band manner e.g. crack propagation in a local region. Nevertheless, it is still necessary to track the crack path so that the inter-element continuity of a discontinuity can be enforced. This can be carried out by a common block which is accessible to all user elements, within which the geometric information of a discontinuity can be constantly updated as it propagates. Herein, a local tracking algorithm based on element connections/graph is adopted in numerical implementation. When an element meets the criterion, the discontinuity propagates within that element along a straight line with the determined orientation, from the discontinuity starting intersection to the end one. Fig. 3 presents the cracked

element topology for different approaches including XFEM, the ECDE and CZM. It can be seen from Fig. 3 that the ECDE (Fig. 3b) is only with standard DoFs **u**, while for XFEM (Fig. 3a), an additional DoFs **a** is contained at each node. In the case of CZM shown in Fig. 3c, although all the nodes are with the standard DoFs, the embedding cohesive element requires the introduction of new nodes, which essentially increases the number of DoFs in a FE model. The approximations of the element deformation on the presence of a crack using different schemes are also illustrated in Fig. 3. In the ECDM scheme, the nodal displacements can be solved accurately, but the physical displacement gap (the dash lines in Fig. 3b) cannot be presented by nodal displacements, instead, it can be presented by a strain field with a distinguished value.

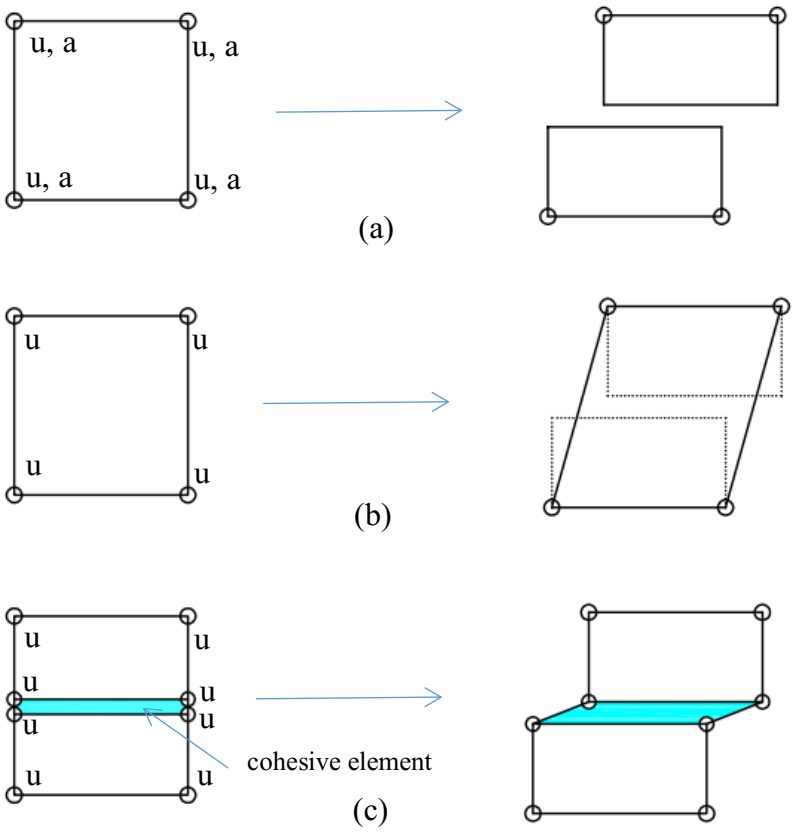

Fig. 3. The characterization of crack by different approaches: (a) XFEM, (b) The ECDE and (c) CZM.

Identifying the element in which discontinuity propagates and establishing the discontinuity configuration are required at the beginning of tracking discontinuity propagation. Determination of discontinuity nucleation is the first work. Nucleation is allowed to happen within any potential elements in the computationally accounted domain, whereas the propagation is originated at the front element of an existing discontinuity tip. In the numerical implementation, a discontinuity nucleation in an element is accounted at its midpoint where the maximum principal stress is over the damage criteria. The perpendicular direction to the direction of the maximum principal stress is determined as the crack direction. The determined crack starts from the middle point and ends at the edge of the cracked element through a straight line along the crack direction. In the case of

existing cracks, normally, the existing crack should propagate to the element at the front of the crack tip. In the case of the cracked element at the boundary of computational domain, only one tip point will be presented. Fig. 4 shows the crack propagation scheme in the ECDE implementation in which the red line is an existing crack. Considering the situation in Fig. 4(a), if the stress state of the element at the front crack tip satisfies the failure criterion, then the existing crack propagates across that element. Thus, the previous crack tip is recognized as a start point of the crack in the new cracked element. A restriction given by a kinking angle between 45^0 and -45^0 degree measured from the existing crack direction provides a potential propagation area as shown in the blue area in Fig. 4. Assuming a crack propagates along a straight line within the failed element, once the coordinates of the start point of the new crack is known, the end point of the crack can be trivially determined in terms of the continuity of the cracking path and the propagating orientation. This can be seen in Fig. 4(b). When a crack propagation in an element is approximated, the discontinuity information will be updated for evaluating other elements.

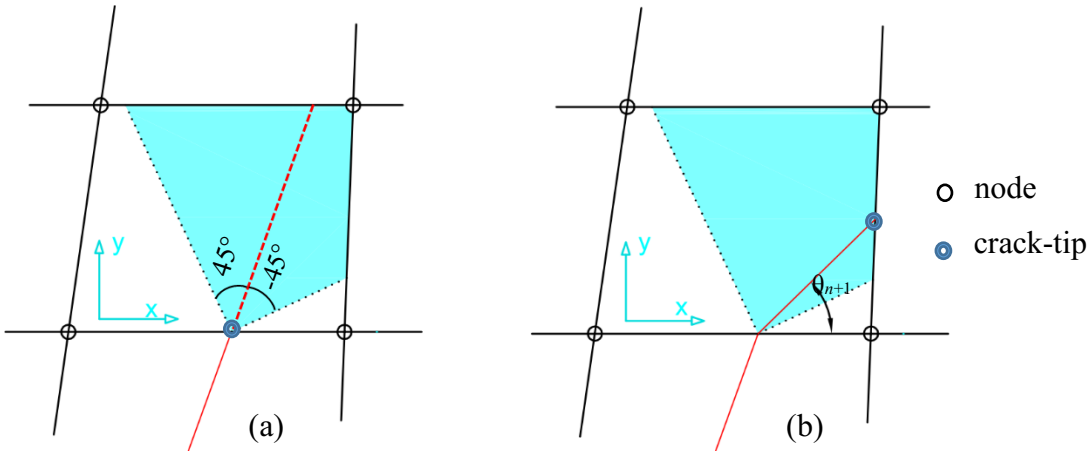

Fig. 4. The crack propagation scheme in the ECDE implementation.

In the implementation of the most discrete discontinue approaches such as XFEM, in order to avoid introducing new DoFs into non-equilibrium states (e.g., in an iterative procedure) and to preserve the quadratic convergence rate of the Newton–Raphson scheme, the propagation is accounted after the iterative procedure performed [27]. Consequently, the increment size must be sufficiently small during loading process, especially around the loading point of material failure, so as to capture the peak value and to avoid overestimation of element strength. In this work, attributing to the elimination of enriched DoFs, discontinuities are allowed to be initiated before iteration in the increment rather than at the end of a converged loading increment, which identifies with the normal nonlinear solving procedure and obtains accurate result even if relatively coarse increment size is used.

The discontinuity propagation procedure according to the theoretical formulations of the ECDE presented in Section 2 has been implemented into FEM package ABAQUS by a user element UEL. Fig. 5 shows the flow chart of the UEL which uses the information for existing cracks, trail incremental displacements applied to the structure at the start of increment *n,* and the trail stress $\boldsymbol{\sigma}$ at the front

of crack-tip of the identified element for evaluating crack propagation. If a crack is judged to propagate, the elemental crack configuration will be updated with computed new crack orientation and geometric information of previous crack tip. The updated crack information includes the location of the crack within the individual element and, in particular, the nodes for the starting and end points of the crack located at elemental edges. Subsequently, the element stiffness matrix and the nodal residual force can be updated according to Equ. (15) or Equ. (17). In general route to solve nonlinear equilibrium equations, the Newton-Raphson iteration method associated with line search algorithm is performed. When the residual nodal force reduces to the prescribed tolerance, the convergent solution is obtained, subsequently the computing process moves to increment *n+1* with newly updated crack information. In the case of convergent failure, the computing system will automatically adjust the size of increment *n*, and repeat above procedure using the crack information backed up at the end of increment *n-1*, until reaching the convergent solution. Since the crack is tracked in real time and each element can access crack information at any time, the crack can propagate through more than one element within one increment.

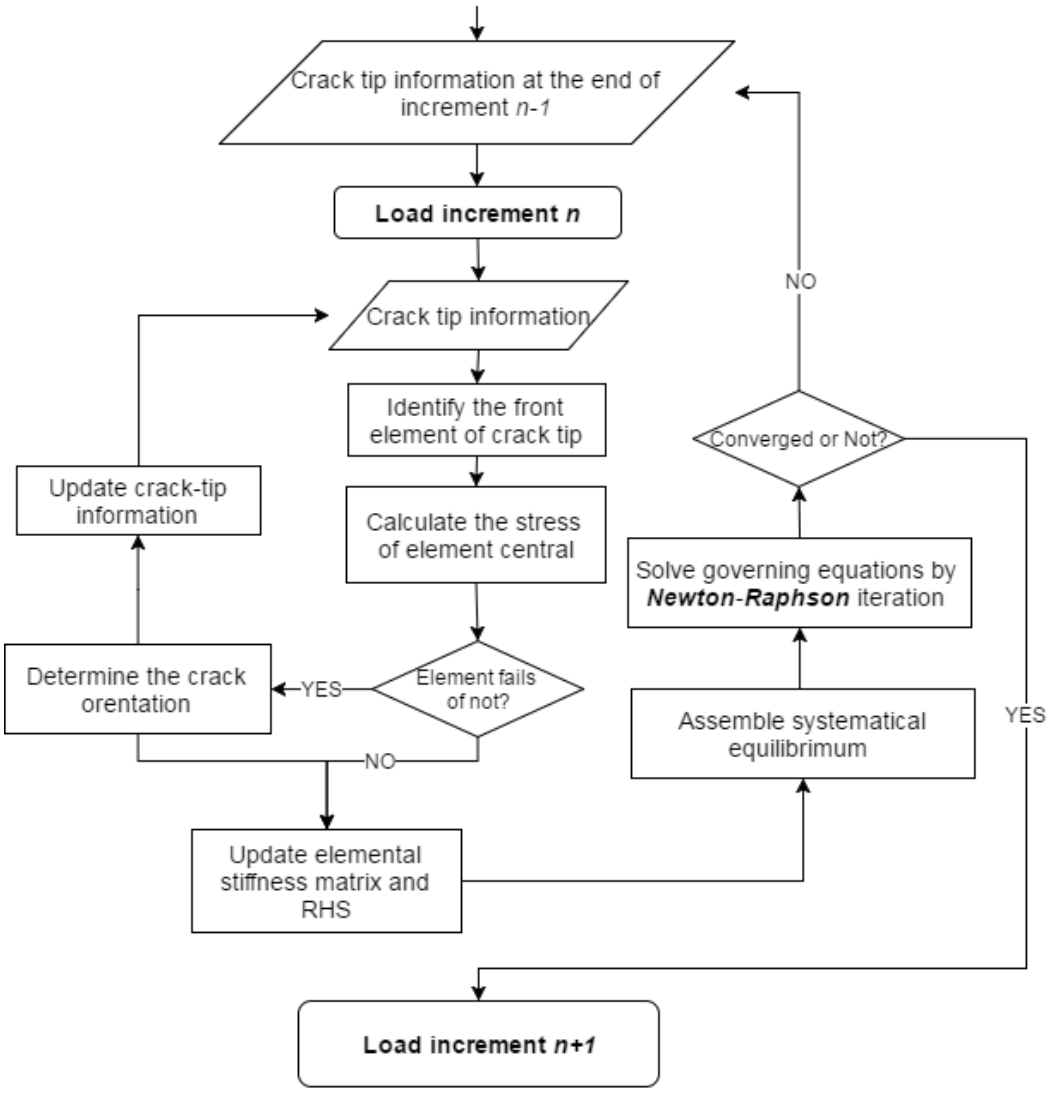

Fig. 5. The flow chart of crack propagation scheme and solving procedure in the ECDE.

4. Snow materials

Snow is a porous material consisting of crystalline ice particles (or grains) welded together. The microstructure scale is of the order of 10^{-4} m. The microstructure describes the size, shape, and arrangement of grains that cannot be seen by the naked eye. Classical snow characterization using a 10-power hand lens focuses on grain type and size. The mechanical properties are determined by the arrangement of grains and particularly by the size and number of bonds as well as related density. Whereas the term microstructure is commonly used in engineering, an alternative term (snow texture) is more commonly used in the geosciences. Snow can be considered as cellular solid rather than as a granular material. It is a sintered material, and for low densities has foam-like properties. However, as the microstructure changes with increasing density, the foam concept is probably not applicable for the whole density range (50–500 kg m^{-3}) of seasonal snow. Although Voitkovsky et al. in 1975 showed that cohesion correlated better with specific grain contact surface (total cross-sectional area of the bonds per unit bulk area) than with density. There are not many publications to investigate the effects of snow microstructure on properties [31, 35]. Several papers reported snow material properties varying with densities [28 - 33]. Snow material properties considered as a function of snow density is used in this paper. Material properties of two types of snow, e.g., slab and weak layer, taken or estimated using figures or data from [4, 28, 29, 34, 35] are given in Table 1, and used in the ECDE modelling predictions. It should be noticed that the compressive strength σ_{cc} and crushing toughness G_{cc} are proposed as new items for assessing compression caused damage initiation and propagation. So far there are no reports on testing their values in literature. Their values used in this investigation are estimated through back analysis using the ECDE on the PST example, considering its initial crack length related critical bending moment.

Table 1. Snow material properties

Snow type	Slab	Weak layer
Density ρ (kgm^{-3})	159	100
Young's modulus E (MPa)	2	1
Poisson's ratio ν	0.3	0.3
Friction coefficient β	0.5	0.5
Tensile strength σ_{nc} (MPa)	0.00075	0.000484
Shear strength σ_{tc} (MPa)	0.0011	0.00071
Compressive strength σ_{cc} (MPa)	0.0026	0.00166
Tensile fracture toughness G_{nc} (N/mm)	0.003	0.00075
Shear fracture toughness G_{tc} (N/mm)	0.00015	0.0000375
Crushing toughness G_{cc} (N/mm)	0.06	0.015

5. Damage modes and mixed mode damage criteria

Slab avalanches have the characteristic appearance of a block (slab) of snow cut out from its surroundings by fractures. Elements of slab avalanches include the following: a crown fracture at the top of the start zone, flank fractures on the sides of the start zones, and a mixed mode failure at the bottom called the stauchwall. The crown and flank fractures are vertical walls in the snow delineating the snow that was entrained in the avalanche from the snow that remained on the slope. Fractures

in slab avalanches are obviously mixed mode damage. Crown fracture is a tensile or mode I crack. Flank fracture is shear or mode II crack. The failure at the bottom between slab and weak layer is mixed mode damage with compressive crushing and shear crack. Accordingly, and based on observation, it is proposed that failure initiation at the base of a snow slab is an interfacial mixed mode damage between two snow layers that are poorly connected. For a thin weak layer, the mixed mode damage should start at the interface with the layer above or below. However, for mixed mode damage propagation the full thickness of the weak layer can be involved. Prior to the release of a slab avalanche, conditions for tensile crown and shear flank fractures and mixed mode damage propagation in the weak layer must be met. After fracture or damage initiation the slab would release if slab self-weight related driving force is able to overcome bed surface friction. Therefore, there are three stages in slab avalanche propagation. The first stage is damage initiation in which self-weight and external action related driving force causes internal stress state reached the stress based damage criteria. Damage accumulates during load action period especially external actions, e.g., storm and skiing. A hybrid stress-based criterion for damage initiation is proposed as in Equ. 23.

$$\frac{\sigma_n^2}{\sigma_{nc}^2} + \frac{\sigma_t^2}{\sigma_{tc}^2} + \frac{\sigma_c^2}{\sigma_{cc}^2} = 1 \qquad (23)$$

where, σ_n, σ_t and σ_c are snow tensile, shear and compressive stress respectively. σ_{nc}, σ_{tc} and σ_{cc} are their critical values or strengths. When considering tensile damage initiation on the top of slab, σ_n dominates Equ. 23 for making contribution in damage initiation and accumulation, σ_t would have effect due to coupled correlation, and σ_c should not be available. In dealing with shear damage initiation on both sides of slab, σ_t is mainly accounted as a dominated role, σ_c would have contribution, and σ_n is ignored. Meanwhile, both σ_c and σ_t plays important roles in the mixed mode damage initiation in the bottom of slab or weak layer, σ_n should be removed in this case. The second stage is fracture or damage propagation in which the fracture toughness based criteria is reached due to damage accumulation. A fracture toughness based criterion is proposed to assess the fracture or damage propagation in the slab, which is shown in Equ. 24.

$$\frac{G_n^2}{G_{nc}^2} + \frac{G_t^2}{G_{tc}^2} + \frac{G_c^2}{G_{cc}^2} = 1 \qquad (24)$$

where, G_n, G_t and G_c are strain energy release rates for tensile, shear and compressive cases. G_{nc} and G_{tc} are corresponding critical values, i.e., fracture toughness for tensile and shear cases. G_{nc} and G_{tc} are used to assess the tensile and shear dominated fracture propagation on top and both sides of slab respectively. In these two individual cases, Equ. 24 is simplised as $G_n = G_{nc}$ and $G_t = G_{tc}$ respectively. G_{cc} is a new item, defined as a crushing toughness to assess compression caused damage propagation, G_{cc} together with G_{tc} is used to judge mixed mode damage propagation with coupling effects from crushing damage and shear crack. Thus, Equ. 24 is changed to Equ. 25 to evaluate the mixed mode damage propagation in the weak layer.

$$\frac{G_t^2}{G_{tc}^2} + \frac{G_c^2}{G_{cc}^2} = 1 \quad (25)$$

It is noticed that the mixed mode damage propagation with crushing damage evolution in the weak layer is so called “anticrack” by previous researchers [4, 34] considering its failure phenomena is in the opposite way of opening cracking in terms of the concept of physical fracture meaning. However, crushing can be treated as one type of damage due to compression in damage mechanics based approach, thus the term of “anticrack” can be avoided. Values of all parameters given in Equs. 23 and 24 are shown in Table 1 for ECDE modelling simulation of PST sample in the next section. It should be noticed that Equs. 23 and 24 are the proposed second order functions based criteria for judging damage initiation and propagation. Similar criteria are commonly used in analysis of crack propagation in engineering materials [36-38]. However, the crushing damage item introduced in Equs. 23 and 24 is the first time to deal with the mixed mode damage propagation in the weak layer snow slab. In the third stage, because the slab has been cut off by multiple cracks on top and both sides, and the mixed mode damage on the bottom of slab from surrounding snow, a simple condition for slab sliding is slab self-weight related driving force overcoming the bed surface friction. Equ. 26 shows the minimum required driving force P to make slab sliding.

$$P - F_r = 1 \quad (26)$$

where, F_r is the frictional resistance and calculated as: $F_r = W_n \times \beta$, W_n is self-weight component normal to the bed surface, β is the friction coefficient in weak layer or interface between slab and weak layer. It should be noticed that prediction for fracture or damage initiation and propagation in the first and second stages respectively are crucial work in forecasting slab avalanches under external loading conditions, e.g., storm and skiing. The third stage is a relatively simple judgement according to snow terrain slope, snow density and friction coefficient.

6. Numerical applications

The propagation saw test (PST) shown in Fig. 6 is an example used in this paper to demonstrate the application of ECDE in studying damage mechanisms, failure modes and failure response of PST under self-weight related bending, and sliding under driving force to overcome bed surface friction. Fig. 6 shows schematical experimental set-up of PST [4]. After reaching the artificial critical crack length (red star in Fig. 6), the crack propagates from the top of the slab along a mostly vertically line to the interface between the slab and weak layer, and mixed mode damage - sliding along the weak layer. Black markers in Fig. 6 are inserted in the slab and the substratum to track their positions using Particle Tracking Velocimetry [4]. All dimensions of the PST sample studied in this paper shown in Fig. 6 are given in Table 2. Parameters L, D and b can be seen from Fig. 6. In the table 2, D_w is thickness of weak layer, D_s is thickness of substratum and a_c is an artificial critical crack length to form a self-weight related bending. It should be noticed that the slope angle ψ is given zero in this investigation to model example 3 in PST experimental work [4]. This case can clearly explore the

applied bending moment causing multiple crack and damage propagation in snowpack and driving force forming sliding in the weak layer.

Table 2, dimensions of the set-up of PST

L (mm)	b (mm)	D (mm)	D_w (mm)	D_s (mm)	ψ (^{0})	a_c (mm)
1200	300	260	10	60	0	265

According to the dimensions of the PST sample, a plain strain model shown in Fig. 7a is created using dimensions and material parameters provided in Tables 1 and 2 as a basic model to study the PST multiple damage and sliding mechanisms. It should be noted that the whole mesh in Fig. 7a consists of ECDE elements. The bottom of the substratum in PST model is fixed. Material properties for the slab are assigned to the upper mesh with 260 mm thickness and substratum layer with 60 mm thickness. Weak layer material properties are assigned to the layer with 10 mm thickness between slab and substratum. From Fig. 7a, it can be seen an initial critical crack length of 265 mm is created, which induces a self-weight related bending moment. It is noticed that potential damage areas after critical crack length are relatively high mesh density, shown in Fig. 7a.

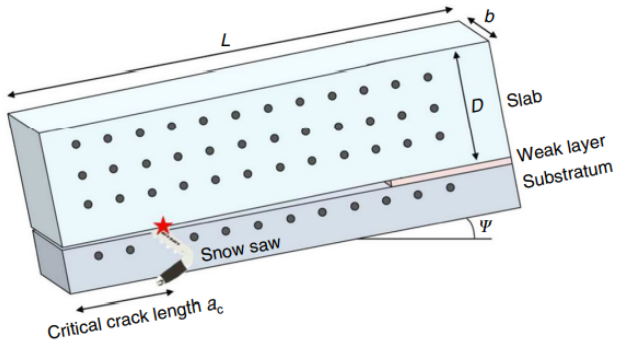

Fig. 6, Schematical experimental set-up of PST [4]

The ECDE modelling of PST has two loading steps to model self-weight related bending and sliding over friction. Each loading step is increased as a quasi-static process from 0 to 1 time history. The first step causes tensile fracture from the top to weak layer of the snowpack and mixed mode damage with compressive crushing and shear crack in the weak layer. The second step is pulling force against the friction to let the cut off snowpack slide on the substratum. The loading is displacement control to investigate self-weight bending scale for causing damage initiation and propagation from the top and in the weak layer progressively. The ECDE modelling is one go with two loading steps. Fig. 7 proves the ECDE predicted deformation to multiple damage propagation in PST shown in Figs. 7b to 7h. Fig. 7b shows a slight deformation of PST under bending moment M = 85 Nmm. There is no damage in the PST model. Fig. 7c shows a deformation with tensile damage initiation on the top of snowpack under M = 1410 Nmm, and the weak layer under compression. The potential tensile crack is at the location of 135 mm horizontal distance from the front of initial critical crack. Fig. 7d shows slab tensile crack propagation along the vertical line from the top with a released M = 92.5 Nmm from the previous crack initiation related bending moment (refer to Fig. 9 failure response), the

weak layer under compression. Fig. 7e shows slab tensile crack propagation through the vertical line from top to the weak layer under M = 4370 Nmm. This bending moment is a peak value to cause the final tensile fracture in the snowpack, which can be seen from the failure response in Fig. 9. It should be noticed that the tensile crack propagation from the top to the weak layer is rather quick which agrees with test observation. Meanwhile, the weak layer is damaged by compressive crushing and shear crack, which can be seen from Fig. 7f, presented by the expanded mesh penetration in the weak layer.

In the second loading stage, Fig. 7g shows that the slab starts largely sliding because the snow weak layer is totally damaged by crushing damage and shear crack, the force F = 16.8 N overcame the friction to drive the slab slide, and strain – stress state in the snowpack caused by bending in the loading step 1 is mostly released. Fig. 7h shows the final stage of the slab sliding within the given displacement. Fig. 8 shows a PST image with an initial saw crack and the bending caused tensile crack from the top of slab and the final tensile crack and mixed damage with crushing and shear crack in the weak layer [4]. It should be noticed that the PST work in [4] only provided crack images and calculated deformation and velocity of sliding speed after slab fractured from snowpack. This information would not be directly used for estimating external loads causing fracture or damage in the snowpack.

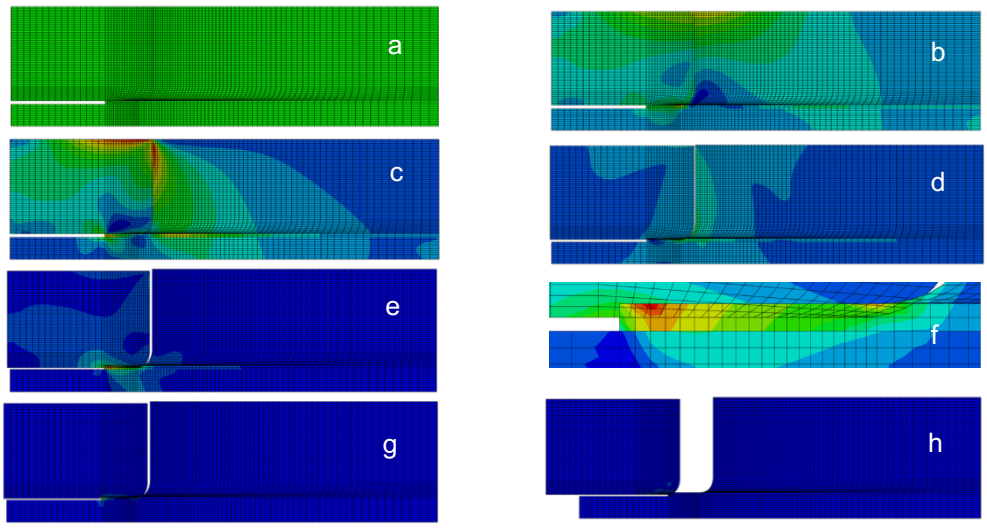

Fig. 7, Multiple mixed mode damage propagation of PST under self-weight related bending and sliding driven by the force against friction

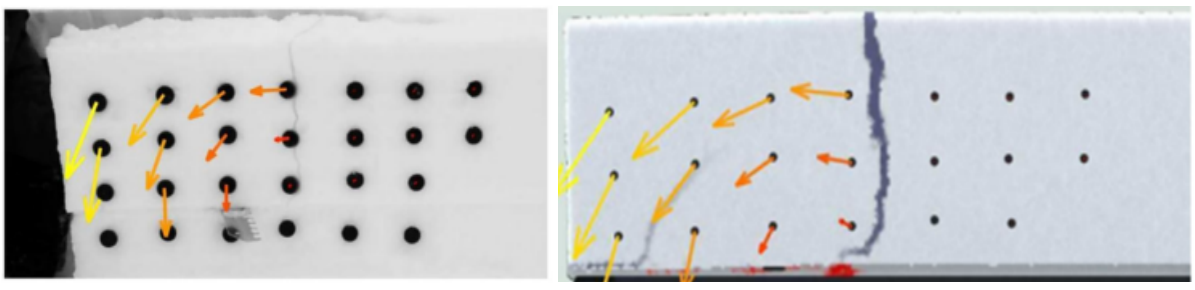

Fig. 8, PST images showing bending caused multicrack propagation in the snowpack [4]

The multiple mixed mode damage response under bending in the first loading step can be seen from Fig. 9. The peak value of the bending moment in the response curve is 4370 Nmm which is recognised as the driving moment to cause tensile crack from the top of snowpack. This moment value is slightly higher than the self-weight related bending moment 4266 Nmm (calculated using the bulk mass of the slab fractured from snowpack, mass density and half of the initial critical crack length) applied in the initial critical crack front related cross section. Fig. 9 also shows two dropping points which reflect the feature of porous materials' unstable crack propagation, one before and one after the peak value of failure bending moment. The resultant displacement given in loading step 1 is about 1.8 mm, Fig. 9 shows a crucial period of damage propagation which indicates correlation between bending moment and displacement before 0.75 mm, the rest part of response is almost zero bending moment because tensile crack goes through the path from the top to the weak layer. The self-weight related bending moment also caused the mixed mode damage with compressive crushing and shear in the weak layer, which can be seen from Fig. 7f. Fig. 10 shows the shear cracking - Sliding response in the second loading step. Controlled displacement continues from 1.8 mm at the end of loading step 1. The peak value of 16.8 N exceeds the frictional resistant 16.1 N (calculated using the bulk mass of the slab fractured from snowpack and frictional parameter). The pick value of driving force would also include part of shear crack propagation related force before sliding. Fig. 10 also shows an unstable damage response with other two drops in early stage of sliding to cope with shear crack propagation and frictional resistance. The crucial response period in the controlled displacements is from 1.8 mm to 10 mm. After that the shear force resistance come down to zero because the fractured slab slides through the path of controlled displacement with the maximum value of 135 mm.

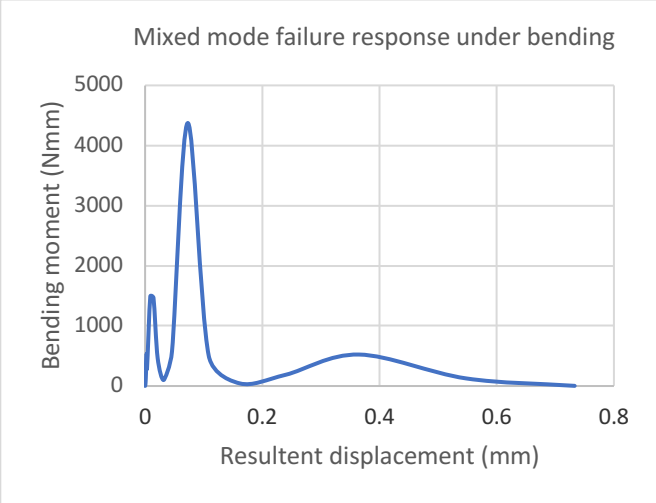

Fig. 9, Multiple mixed mode damage propagation under bending

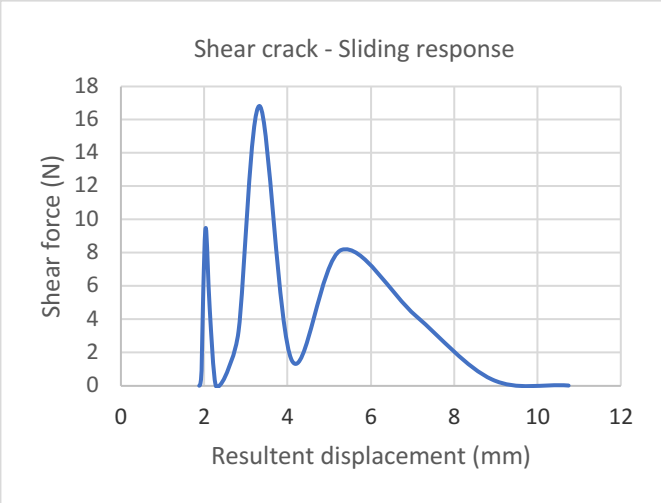

Fig. 10, Shear crack - Sliding against friction

It should be noticed that the detailed mixed mode damage propagation and shear – sliding in the weak layer in the loading steps 1 and 2, presented by expanded mesh penetration and slab movement, can be seen from Figs. 11 and 12 respectively. Figs. 11a to 11e show the mixed mode damage propagation in the weak layer in the varied loading history of bending moment: a) the weak layer under compression without damage; b) the weak layer initially damaged presenting by mesh penetration on the top of weak layer; c) weak layer significantly damaged from the top; d) the weak layer damaged further from the top; e) the weak layer damaged through half weak layer thickness from the top. Figs. 12f to 12j show the shear crack propagation – slab sliding in the weak layer in the varied loading history of shear force: f) the weak layer damaged with more shear crack presented by slab (the upper mesh) moving towards the left side; g) the weak layer damaged further by shear and more slab moving; h) the slab sliding further driven by the force overcoming the friction; i) the slab sliding significantly; j) the slab sliding through the weak layer length.

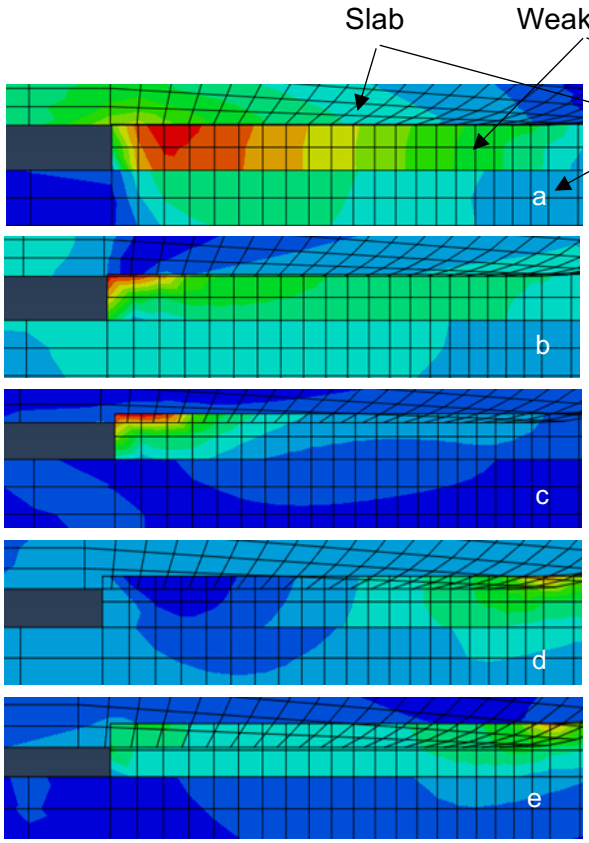

Fig. 11a to 11e, Bending caused mixed mode damage propagates in the weak layer

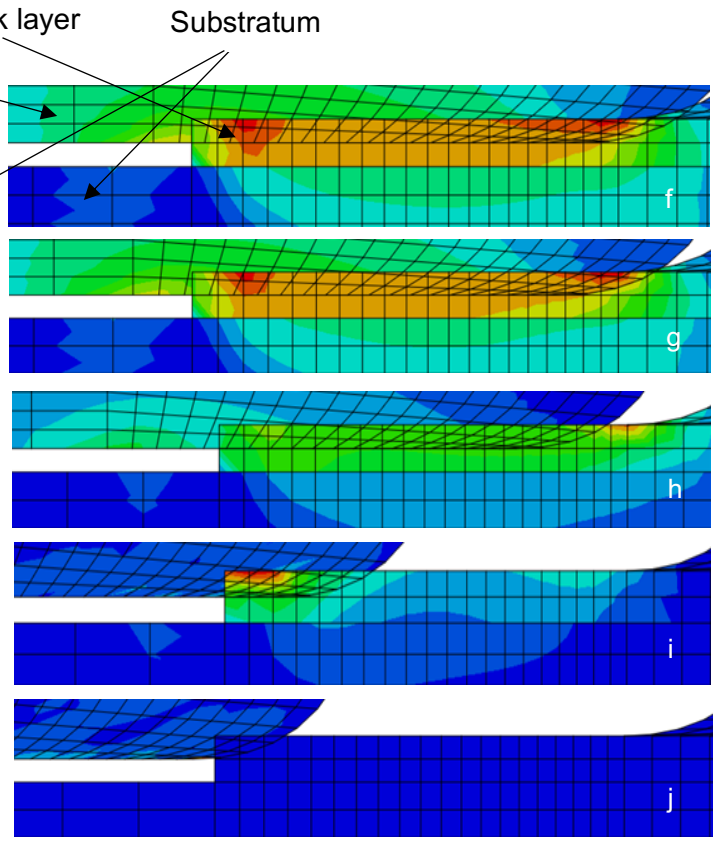

Fig. 12f to 12j, Shear crack propagation – Slab sliding towards the left side of the weak layer.

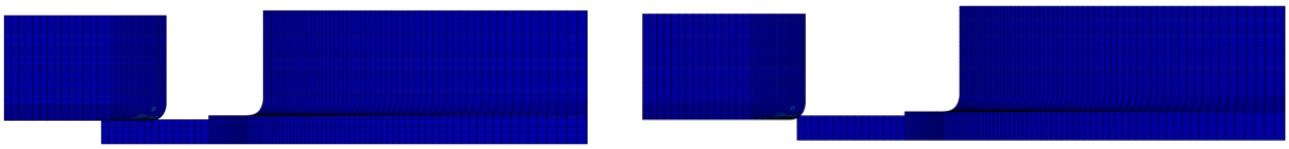

Fig. 13, The ECDE simulated whole fracture propagation of the weak layer in the PST

In an additional modelling in this paper, the ECDE is used to simulate the whole fracture propagation of the weak layer from the mixed mode damage propagation to sliding to the end of the PST sample, which can be seen from Fig. 13. Fig. 13a shows the slab sliding further along the initial crack surface. Fig. 13b show the slab sliding to the end of the PST beam. It should be noticed that the position of sliding slab at the end of PST beam should be re-calculated using kinematic dynamic approach through post process considering its rotating downward driven by gravity to follow experimental observation. Although this post process is out of the scope of the ECDE it can be developed by a post treatment algorithm. It should also be noted that the PST in slope case in [4] can be simply treaded by changing the angle of snowpack then repeat the simulation under self-weight related driving force together with bending moment, its damage mechanisms are similar to the zero-angle case in this investigation thus not included considering the length of the paper.

7. Conclusions and future work

The ECDE equations together with a novel mixed mode damage criterion for snowpack fracture analysis are introduced in this paper. The ECDE based modelling is applied to predict failure modes and failure response of the snow PST sample. The predicted failure modes shown in Fig. 7 agrees well with tested images of the PST shown Fig. 8. The ECDE prediction provides multiple damage response (Fig. 9) of the PST sample under self-weight related bending to cause tensile fracture from the top and the mixed mode damage in the weak layer of the snowpack, and the shear crack – slab sliding response (Fig. 10) in the weak layer under the pulling force overcoming the friction. The predicted failure responses have explored the correlations between applied loads and corresponding failure modes. And these correlations with failure loads can be used in forecasting snow avalanches under external loads, e.g., snowstorm, strong wind and skiing activities. It can be seen from the ECDE simulation of the PST example that the novel mixed mode damage criterion with introduced new item of crushing damage energy together with shear damage energy is able to reflect the mixed mode damage propagation in the weak layer, which can be seen from Fig. 11 and 12. It should be also noticed that the ECDE based nonlinear damage modelling of PST with snow porous materials is rather efficient, its CPU time is less than 100 seconds. This is a good indication for the ECDE applying in large scale modelling of snow terrains for real time snow avalanche alerting where computational speed is one of the paramount factors.

Clearly, a great deal of more work is needed to make this new modelling approach into operational snow avalanche forecasting. Future work would include experimental investigation of snow properties, including compressive strength and crushing damage energy, against snow density and micro construction, which can be used in snowpack modelling for precisely assessing their performance, and applications of the ECDE in modelling selected snow terrains to predict avalanches under environmentally related applied loads. The ECDE technology has potential to be used for providing an early warning of avalanches in terms of weather forecast and planned skiing, etc., for helping decision making in the future.

Acknowledgement

Authors appreciate Alec. van Herwijnen at WSL Institute for Snow and Avalanche Research SLF, Switzerland for using their tested data of the PST and discussion on snowpack fracture propagation mechanisms.

References

[1]. Jürg Schweizer, et al., SNOW AVALANCHE FORMATION, Reviews of Geophysics, 41, 4 / 1016, 2003, doi:10.1029/2002RG000123.
[2]. https://doi.org/10.5194/egusphere-egu21-16361, EGU General Assembly 2021.
[3]. https://cordis.europa.eu/project/id/298672
[4]. J. Gaume, T. Gast, J. Teran, A. van Herwijnen & C. Jiang, Dynamic anticrack propagation in snow, NATURE COMMUNICATIONS | DOI: 10.1038/s41467-018-05181-w.
[5]. Durand, Y., G. Giraud, E. Brun, L. Me´rindol, and E. Martin, A computer-based system simulating snowpack structures as a tool for regional avalanche forecasting, J. Glaciol., 45(151), 469–484, 1999.
[6]. Lehning, M., P. Bartelt, R. L. Brown, T. Russi, U. Sto¨ckli, and M. Zimmerli, Snowpack model calculations for avalanche warning based upon a network of weather and snow stations, Cold Reg. Sci. Technol., 30, 145–157, 1999.
[7]. Bader, H., H. U. Gubler, and B. Salm, Distributions of stresses and strain-rates in snowpacks, in Numerical Methods in Geomechanics (Innsbruck 1988), edited by G. Swoboda, pp. 2257–2263, A. A. Balkema, Brookfield, Vt., 1989.
[8]. Bader, H., and B. Salm, On the mechanics of snow slab release, Cold Reg. Sci. Technol., 17, 287–299, 1990.
[9]. Schweizer, J., The influence of the layered character of the snow cover on the triggering of slab avalanches, Ann. Glaciol., 18, 193–198, 1993.
[10]. Wilson, A., J. Schweizer, C. D. Johnston, and J. B. Jamieson, Effects of surface warming of a dry snowpack, Cold Reg. Sci. Technol., 30, 59–65, 1999.
[11]. Schillinger, L., D. Daudon, and E. Flavigny, 3D modelisation of snow slabs stability, in 25 Years of Snow Avalanche Research, Voss, Norway, 12–16 May 1998, vol. 203, edited by E. Hestnes, Norw. Geotech. Inst., Oslo, 1998.
[12]. P. Hagenmuller, G. Chambon and M. Naaim, Microstructure-based modeling of snow mechanics: a discrete element approach, The Cryosphere Discuss., 9, 1425–1460, 2015. doi:10.5194/tcd-9-1425-2015
[13]. M. Christen, J. Kowalski and P. Bartelt, RAMMS: Numerical simulation of dense snow avalanches in three-dimensional terrain, Cold Regions Science and Technology, 63, 1–2, 1-14, 2010.
[14]. Bahram Choubina, et al., Snow avalanche hazard prediction using machine learning methods, Journal of Hydrology, 577, 123929, 2019.
[15]. BABUŠKA, I. and J.M. MELENK (1997) THE PARTITION OF UNITY METHOD. International Journal for Numerical Methods in Engineering, 40(4), 727-758.
[16]. Belytschko, T. and T. Black (1999) Elastic crack growth in finite elements with minimal remeshing. International Journal for Numerical Methods in Engineering, 45(5), 601-620.
[17]. Mo S, N., J. Dolbow and T. Belytschko (1999) A finite element method for crack growth without remeshing. International Journal for Numerical Methods in Engineering, 46(1), 131-150.
[18]. Gigliotti, L. Assessment of the applicability of XFEM in Abaqus for modeling crack growth in rubber. Applied Mechanics, 2012.
[19]. Li, X. and J. Chen (2017) An extended cohesive damage model for simulating arbitrary damage propagation in engineering materials. Computer Methods in Applied Mechanics and Engineering, 315, 744-759.
[20]. X. Li and J. Chen, An extended cohesive damage model for simulating multicrack propagation in fibre composites, Composite Structures, 143, 1–8, 2016.
[21]. X. Li and J. Chen, The implementation of the extended cohesive damage model for multicrack evolution in laminated Composites, Composite Structures, 139, 68–76, 2016.
[22]. X. Li and J. Chen, A highly efficient prediction of delamination migration in laminated composites using the extended cohesive damage model, Composite Structures, 160, 712–721, 2017.
[23]. S. Ghimire, J. Chen, Predicting fracture mechanisms in synthetic foam sandwiches with multi

-layered cores using extended cohesive damage model, Engineering Fracture Mechanics, 223, ID 106719, 2020.
[24]. S. Ghimire, J. Chen, An extended cohesive damage model study of geometrical ratio effects on failure mechanisms of functionally graded sandwiches with multi-layered cores, Composite Structures, 224, ID 110999, 2019.
[25]. Foulk, J.W., D.H. Allen and K.L.E. Helms, Formulation of a three-dimensional cohesive zone model for application to a finite element algorithm. Computer Methods in Applied Mechanics and Engineering, 183(1-2), 51-66, 2000.
[26]. Chen, J. (2014) An extended cohesive damage model with a length scalar in fracture analysis of adhesively bonded joints. Engineering Fracture Mechanics, 119, 202-213.
[27]. Wu, J., F. Li and S. Xu (2015) Extended embedded finite elements with continuous displacement jumps for the modeling of localized failure in solids. Computer Methods in Applied Mechanics and Engineering, 285, 346-378.
[28]. Jurg SCHWEIZER, et al, On the fracture toughness of snow, Annals of Glaciology, 38, 2004.
[29]. Berna KOCHLE and Martin SCHNEEBELI, Three-dimensional microstructure and numerical calculation of elastic properties of alpine snow with a focus on weak layers, Journal of Glaciology, Vol. 60, No. 222, 2014 doi: 10.3189/2014JoG13J220.
[29]. J.B. lAMIESON and C.O. lOHNSTON, IN-SITU TENSILE TESTS OF SNOW-PACK LAYERS, Glaciology, Vol. 36, No. 122, 1990.
[30]. Bruge Jamieson, et al, Evaluation of the shear frame test for weak snow layers, Annals of Glaciology, 32, 2001.
[31]. ALEC VAN HERWIJNEN, et al, Estimating the effective elastic modulus and specific fracture energy of snowpack layers from field experiments, Glaciology, 2016, 62(236), 997–1007, 2016.
[32]. Evgeny Andreevich Podolskiy, et al, A review of finite-element modelling in snow mechanics, Glaciology, Vol. 59, No. 218, 2013 doi: 10.3189/2013JoG13J121.
[33]. Blair Fyffe, Mechanics of snow slab avalanche release, PhD thesis, University of Edinburgh, UK, 2006.
[34]. Philipp L. Rosendahl and Philipp Weibgraeber, Modeling snow slab avalanches caused by weak-layer failure – Part 2: Coupled mixed-mode criterion for skier-triggered anticracks, The Cryosphere, 14, 131–145, 2020.
[35]. A. van Herwijnen and B. Jamieson, Snowpack properties associated with fracture initiation and propagation resulting in skier-triggered dry snow slab avalanches, Cold Regions Science and Technology 50, 13–22, 2007.
[36]. J. Chen, M. Crisfield, A. J. Kinloch, et al, Predicting progressive delamination of composite material specimens via interface elements, *Mechanics of Composite Materials and Structures*, Vol. 6, Number 4, 301-317, 1999.
[37]. Kinlock A. J., Wang Y., J. G. Williams, et al., The mixed-mode delamination of fibre composite materials, *composite science and technology*, 47, pp. 225-237, 1993.
[38]. Tvergaard V. and Hutchinson J. W., The influence of plasticity on mixed mode interface toughness. J. Mech. Phys. Solids 41, pp. 1119-1135, 1993.